Zhao *et al. Chin. J. Mech. Eng.* (2020) 33:67
https://doi.org/10.1186/s10033-020-00486-8

Chinese Journal of Mechanical Engineering

ORIGINAL ARTICLE

Open Access

# Cavitation of a Submerged Jet at the Spherical Valve Plate/Cylinder Block Interface for Axial Piston Pump

Bin Zhao[1,2,3*], Weiwei Guo[1] and Long Quan[1,2]

**Abstract**

The spherical valve plate/cylinder block pair has the advantages of strong overturning resistance and large bearing area. However, the configurations of the unloading and pre-boosting triangular grooves on the spherical valve plate are different from those in the planar valve plate, resulting in special cavitation phenomenon on the spherical port plate pair. In order to study cavitation characteristics of spherical port plate pair, a dynamic CFD model of the piston pump including turbulence model, cavitation model and fluid compressibility is established. A detailed UDF compilation scheme is provided for modelling of the micron-sized spherical oil film mesh, which makes up for the lack of research on the meshing of the spherical oil film. In this paper, using CFD simulation tools, from the perspectives of pressure field, velocity field and gas volume fraction change, a detailed analysis of the transient evolution of the submerged cavitation jet in a axial piston pump with spherical valve plate is carried out. The study indicates the movement direction of the cavitation cloud cluster through the cloud image and the velocity vector direction of the observation point. The sharp decrease of velocity and gas volume fraction indicates the collapse phenomenon of bubbles on the part wall surface. These discoveries verify the special erosion effect in case of the spherical valve plate/cylinder block pair. The submerged cavitation jet generated by the unloading triangular grooves distributed on the spherical valve plate not only cause denudation of the inner wall surface of the valve plate, but also cause strong impact and denudation on the lower surface of the cylinder body. Finally, the direction of the unloading triangular groove was modified to extend the distance between it and the wall surface which can effectively alleviate the erosion effect.

**Keywords:** Cavitation submerged jet, Spherical valve plate/cylinder block pair, Axial piston pump

## 1 Introduction

In hydraulic system, cavitation is one of the main reasons that cause mechanical vibration, noise, and deterioration of the reliability and durability of pumps and valves [1–5]. To reduce the effect of cavitation on the hydraulic components, a large number of studies on cavitation phenomenon in high pressure, high rotating speed and high precision hydrodynamic system components have been carried out. Cavitation is defined as the process in which the local pressure of the fluid falls below the saturated vapor pressure, and the gas evolves from the dissolved state to cause erosion [6]. Cavitation will denude mechanical parts, which will lead to a series of chain effects such as abrasive wear, poor sealing effect of components and reduction of load-bearing capacity [7].

The research on cavitation in axial piston pump can be divided into two basic branches [8]: One is the macroscopic study of cavitation in hydraulic pumps, which involves the precipitation and digestion of bubbles and the process of bubble transport with fluid [9], such as cavitation caused by friction loss and local pressure loss of the oil suction pipeline [10], cavitation caused by low oil suction pressure [11, 12], cavitation [10–13]

*Correspondence: zbtyut@126.com
[1] College of Mechanical and Vehicle Engineering, Taiyuan University of Technology, Taiyuan 030024, China
Full list of author information is available at the end of the article

caused by instantaneous increase of piston-cylinder volume while oil fails to fill in time. This kind of cavitation phenomenon can be avoided by increasing the suction oil pressure [14, 15], optimizing the structure of the oil inlet and waist-shaped holes [16, 17], and using a spherical valve plate instead of a planar valve plate [18, 19]. The other hand is to study the cavitation phenomenon caused by micro-jet in the special structure of a piston pump [20]. In the first situation mentioned above, the bubble generation can be attributed to volume expansion, while the bubble generation of the submerged jet is due to the sudden change of the oil flow rate. At present, the cavitation phenomenon caused by the oil flow rate has been studied correspondingly. Ye et al. [21] conducted a transient analysis on the fluid physical characteristics near the damping hole of the valve plate. The evolution process of the damping hole being eroded by the bubble-carrying fluid is explained in detail, and the relationship between the fluid velocity and the erosion area is confirmed. Liu [22] proposed a method to evaluate the cavitation characteristics of the triangular groove of piston pump by analyzing the jet angle at the outlet of the decompression groove. The erosion phenomenon of pre-pressure boosting triangular groove on piston cavity and distribution plate was inferred.

According to the above researches, it can be found that there is a certain relationship between the micro-jet cavitation phenomenon and the structure of the valve plate. At present, the existing submerged jet cavitation researches are all based on the planar distribution plate [23–25]. With the development of high speed, high pressure, and large displacement axial piston pump, spherical valve plate has been applied in the axial piston pumps. However, the research on cavitation phenomenon of spherical valve plate/cylinder block pair is utmost rare at present. On the spherical valve plate/cylinder block pair, there is a height difference between the outer edges and inner edges both on the valve plate and the cylinder block, which will affect the structure of the triangular groove on the valve plate. Therefore, compared with planar valve plate/cylinder block pair, the cavitation phenomenon and erosion must have a certain particularity in the spherical valve plate/cylinder block pair.

Many research results show that in the piton pump, the cavitation phenomena of fluid micro-jet is similar to the high-speed submerged jet. Toshiharu et al. [26] studied cavitation erosion caused by the impact of the hydraulic oil on the plane and grooves. The research results show that the maximum mass loss of cavitation erosion has corresponding best confrontation distance, and the mass loss decreases with the increase of the oil impact angle. Hutli et al. [27–29] used the cavitation submerged jet device to directly observe the cavitation evolution process, obtaining the relationship between erosion rate and hydrodynamic conditions, geometric conditions and fluid properties. The static study of cavitation submerged jet has great guiding significance for understanding and improving sub-merged jet in axial piston pump.

With regard to the current research on the jet phenomenon of the triangular groove, the researchers only captured the moment when the micro-jet is generated, and then rashly inferred the subsequent cavitation phenomenon. In order to study the cavitation phenomenon of flow field under the condition of using spherical valve plate/cylinder block pair, the hydrodynamic hybrid simulation model of a piston pump with spherical valve plate/cylinder block pair is established firstly by using UDF surface modeling technology, which solves the problem that it is difficult to model the fluid domain of micron-level large curvature spherical oil film. Then, reference points near different erosion wall positions are established in the simulation model. The evolution process with cylinder angular displacement of triangular groove jet pressure, velocity and gas volume fraction cloud image is analyzed in detail. In the process, the structural differences between plane valve plate and spherical valve plate are also compared. Finally, by combining the cloud image evolution process with the velocity vector direction and the change of gas volume fraction at the reference points, the simulation results and the experimental results are compared to verify the cavitation damage mechanism of the flow distribution plate and the bottom of the cylinder. Considering the best standoff distance of submerged jet, the deflection angle of triangular groove is changed to extend the standoff distance, and the feasibility of structural optimization is verified from the simulation level.

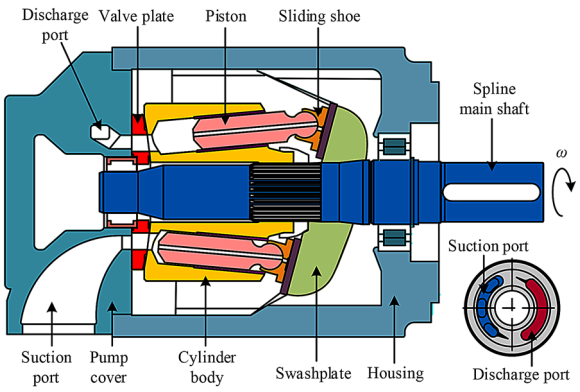


**Figure 1** Schematic diagram of axial piston pump with spherical valve plate/cylinder block pair

## 2 Mathematical Model and Simulation Modeling

The structural diagram of the axial piston pump is shown in Figure 1. The rotor is mainly composed of spline main shaft, cylinder body, piston and sliding shoe, and the stator is mainly composed of housing, swashplate, valve plate, and pump cover. When the splined spindle drives the cylinder body to rotate, 9 pistons will reciprocate in the cylinder body to complete the work of oil suction and discharge. In order to alleviate the hydraulic impact and over-pressure relief of the piston at the top and bottom dead centers during the oil suction and discharge conversion process, a pre-boosting triangular groove and an unloading triangular groove are set on the valve plate. The spherical structure of the valve pair requires that the triangular grooves are arranged obliquely on the spherical surface in a transverse direction. Compared with plane valve plate/cylinder block pair, the spherical valve plate/cylinder block pair increases the bearing area and oil absorption area. Meanwhile, the orientation, high head difference and opening degree of the triangular groove are changed, which is bound to affect the pre-boosting and depressurizing process of the triangular groove.

### 2.1 Computational Fluid Dynamics Mathematical Model

#### *2.1.1 Governing Equations*

The dynamic fluid flow process is governed by the laws of physical conservation. Under constant temperature condition, the fluid moves together with the gas and steam contained in the fluid. The basic integral of mass and momentum conservation of the mixture is expressed as follows:

$$\frac{\partial}{\partial t}\int_{\Omega(t)}\rho \mathrm{d}\Omega+\int_{\sigma}\rho(\boldsymbol{v}-\boldsymbol{v}_{\sigma})\cdot\boldsymbol{n}\mathrm{d}\sigma=0, \tag{1}$$

$$\begin{aligned}&\frac{\partial}{\partial t}\int_{\Omega(t)}\rho\boldsymbol{v}\mathrm{d}\Omega+\int_{\sigma}\rho[(\boldsymbol{v}-\boldsymbol{v}_{\sigma})\cdot\boldsymbol{n}]\boldsymbol{v}\mathrm{d}\sigma\\&\quad=\int_{\sigma}\tilde{\boldsymbol{\tau}}\cdot\boldsymbol{n}\mathrm{d}\sigma-\int_{\sigma}p\boldsymbol{n}\,\mathrm{d}\sigma+\int_{\Omega}\boldsymbol{f}\mathrm{d}\Omega,\end{aligned} \tag{2}$$

where $\Omega(t)$ is the volume of the calculation domain or control volume that changes with time, $\sigma$ is the surface of $\Omega(t)$, $\boldsymbol{n}$ is the normal pointing outward to the surface $\sigma$, $\rho$ is the fluid density, $p$ is the static pressure, $\boldsymbol{f}$ is the force exerting on the calculation domain or control volume, $\boldsymbol{v}$ is the fluid velocity, and $\boldsymbol{v}_{\sigma}$ is the surface motion velocity. Shear stress tensor $\tilde{\boldsymbol{\tau}}$ is a function of fluid viscosity $\mu$ and velocity gradient. For Newtonian fluids, it can be expressed as follows:

$$\tau_{ij}=\mu\left(\frac{\partial u_i}{\partial x_j}+\frac{\partial u_j}{\partial x_i}\right)-\frac{2}{3}\mu\frac{\partial u_{\mathrm{k}}}{\partial x_{\mathrm{k}}}\delta_{ij}, \tag{3}$$

where $u_i$ ($i=1, 2, 3$) is the component of velocity $\boldsymbol{v}$ and $\delta_{ij}$ are Kronecker Delta function.

In order to simulate the flow field characteristics more realistically, the turbulence and steam dynamics physical models should be coupled under the consideration of basic conservation laws.

#### *2.1.2 Turbulence Model*

For high-speed axial piston pumps, the high Reynolds number turbulence model, i.e., the standard $k$-$\varepsilon$ model, should be used for the fluid in the calculation domain. Because the cavitation evolution near the wall is considered, the turbulence model with low Reynolds number should be used for the fluid domain model near the wall. Therefore, RNG $k$-$\varepsilon$ model is used to describe [30].

$$\begin{aligned}&\frac{\partial}{\partial t}\int_{\Omega(t)}\rho k\mathrm{d}\Omega+\int_{\sigma}\rho[(\boldsymbol{v}-\boldsymbol{v}_{\sigma})\cdot\boldsymbol{n}]k\mathrm{d}\sigma\\&=\int_{\sigma}\left(\mu+\frac{\mu_{\mathrm{t}}}{\sigma_{\mathrm{k}}}\right)(\nabla k\cdot\boldsymbol{n})\mathrm{d}\sigma+\int_{\Omega}(G_{\mathrm{t}}-\rho\varepsilon)\mathrm{d}\Omega,\end{aligned} \tag{4}$$

$$\begin{aligned}&\frac{\partial}{\partial t}\int_{\Omega(t)}\rho\varepsilon\mathrm{d}\Omega+\int_{\sigma}\rho[(\boldsymbol{v}-\boldsymbol{v}_{\sigma})\cdot\boldsymbol{n}]\varepsilon\mathrm{d}\sigma\\&=\int_{\sigma}\left(\mu+\frac{\mu_{\mathrm{t}}}{\sigma_{\varepsilon}}\right)(\nabla\varepsilon\cdot\boldsymbol{n})\mathrm{d}\sigma\\&\quad+\int_{\Omega}\left(c_1G_{\mathrm{t}}\frac{\varepsilon}{k}-c_2(RNG)-c_2\rho\frac{\varepsilon^2}{k}\right)\mathrm{d}\Omega.\end{aligned} \tag{5}$$

Compared with the standard $k$-$\varepsilon$ model, the RNG model adds a condition, namely $c_2(RNG)$, which is defined as follows:

$$c_2(RNG)=c_2+\frac{C_{\mu}\eta^3\left(1-\eta/\eta_0\right)}{1+\beta\eta^3}. \tag{6}$$

The strength strain $\eta$ is calculated by the following equation.

$$\eta=\frac{k}{\varepsilon}\sqrt{P}. \tag{7}$$

The empirical constants $c_1$, $c_2$, $\sigma_k$, and $\sigma_\varepsilon$ are 1.44, 1.92, 1, and 1.3, respectively. The empirical constants $\eta_0$ and $\beta$ of RNG model are 4.38 and 1.92, respectively. $k$ is turbulent kinetic energy; $\varepsilon$ is the turbulence kinetic energy dissipation rate; $\mu$ is the fluid viscosity; $P$ is the local pressure value.

#### 2.1.3 Cavitation Model

The cavitation model is a key physical model for studying the change process of liquid phase under pressure change conditions. The original cavitation model proposed by Singhal et al. [31] describes the steam distribution as shown in Eq. (8):

$$\frac{\partial}{\partial t}\int_{\Omega(t)}\rho f \mathrm{d}\Omega + \int_{\sigma}\rho[(\boldsymbol{v}-\boldsymbol{v}_{\sigma})\cdot\boldsymbol{n}]f\mathrm{d}\sigma = \int_{\sigma}\left(D_{\mathrm{f}}+\frac{\mu_{\mathrm{t}}}{\sigma_{\mathrm{f}}}\right)(\nabla f\cdot\boldsymbol{n})\mathrm{d}\sigma + \int_{\Omega}(R_{\mathrm{e}}-R_{\mathrm{c}})\mathrm{d}\Omega, \tag{8}$$

where $\Omega(t)$ is the volume of the calculation domain or control volume that changes with time, $\sigma$ is the surface of $\Omega(t)$, $\boldsymbol{n}$ is the normal pointing outward to the surface $\sigma$, $\rho$ is the oil density, $f$ is the mass fraction of steam, $\boldsymbol{v}$ is the fluid velocity vector, $\boldsymbol{v}_{\sigma}$ is the surface motion velocity vector, $D_{\mathrm{f}}$ is the vapor diffusion rate, $\mu_{\mathrm{t}}$ is turbulent viscosity, $\sigma_{\mathrm{f}}$ is Prandtl number, steam precipitation $R_{\mathrm{e}}$ and digestion rate $R_{\mathrm{c}}$ are respectively expressed as following equations.

$$R_{\mathrm{e}} = C_{\mathrm{e}}\cdot\rho_{\mathrm{l}}\rho_{\mathrm{v}}\left[\frac{2}{3}\frac{(p-p_{\mathrm{v}})}{\rho}\right]^{\frac{1}{2}}(1-f_{\mathrm{v}}-f_{\mathrm{g}}), \tag{9}$$

$$R_{\mathrm{c}} = C_{\mathrm{c}}\cdot\rho_{\mathrm{l}}\rho_{\mathrm{v}}\left[\frac{2}{3}\frac{(p-p_{\mathrm{v}})}{\rho}\right]^{\frac{1}{2}}f_{\mathrm{v}}, \tag{10}$$

where $C_{\mathrm{e}}$ and $C_{\mathrm{c}}$ are cavitation evaporation and condensation coefficients, respectively (the best $C_{\mathrm{e}}$ and $C_{\mathrm{c}}$ are obtained through hundreds of permutation and combination simulations, taking 0.02 and 0.01 respectively). $\rho_{\mathrm{l}}$ and $\rho_{\mathrm{v}}$ are density of steam and gas, respectively. $p$ and $p_{\mathrm{v}}$ are liquid pressure and vapor pressure, respectively. $f_{\mathrm{v}}$ and $f_{\mathrm{g}}$ are mass fraction of steam and gas respectively.

In the full cavitation model, the working fluid is assumed as a mixture of liquid, vapor and non-condensable gas. The density of the mixture is expressed by the following equation:

$$\frac{1}{\rho} = \frac{f_{\mathrm{v}}}{\rho_{\mathrm{v}}} + \frac{f_{\mathrm{g}}}{\rho_{\mathrm{g}}} + \frac{1-f_{\mathrm{v}}-f_{\mathrm{g}}}{\rho_{\mathrm{l}}}, \tag{11}$$

where $\rho_{\mathrm{g}}$ is the gas density. Then the gas volume fraction $\alpha_{\mathrm{g}}$ and the steam volume fraction $\alpha_{\mathrm{v}}$ are calculated by the following equation:

$$\alpha_{\mathrm{g}} = \frac{f_{\mathrm{g}}\rho}{\rho_{\mathrm{g}}}, \tag{12}$$

$$\alpha_{\mathrm{v}} = \frac{f_{\mathrm{v}}\rho}{\rho_{\mathrm{v}}}. \tag{13}$$

### 2.2 CFD Model Grid Establishment

Reasonable design and high-quality generation of fluid domain grids are prerequisites for simulation calculation. The oil film has a considerable influence on the performance of the piston pump, and the oil film of the piston-cylinder pair is the main internal leakage mode in the piston pump. Therefore, compared with the previous three-dimensional CFD modeling without considering the lubricating oil film, the whole pump internal flow field model in this study can more accurately and completely simulate the three-dimensional complex flow state inside the pump. The existence of the oil film will definitely affect the triangular groove unloading efficiency, thus further affecting the jet state. For the spherical oil film between valve plate and cylinder block, because the thickness of the oil film is micron-sized and has a spherical structure with large curvature, the method of drawing and exporting the fluid domain by three-dimensional mapping software is not applicable. On the one hand, the generation of grid is completed on the basis of STL file, which uses a limited number of polylines when expressing the spherical surface. The first approximation is formed in the process. Secondly, the generation of spherical mesh is the best approximation to the STL file's shape, which forms the second approximation of the mesh shape. Therefore, the accuracy of the mesh generated by this method must be quite different from the actual situation, making it more difficult to accurately represent the spherical curvature of the oil film. In this study, the UDF function mesh transformation method is adopted. In the PumpLinx software, the specified area of the plane oil film is modified according to relational expression. The spherical surface is formed by continuously modifying the actual position of the next mesh node. The accuracy of the spherical curvature can be improved by increasing the density of the grids. The three-dimensional binary tree Cartesian grid of the

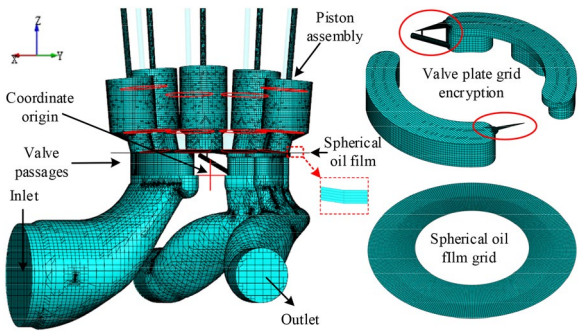


**Figure 2** Three-dimensional whole pump binary tree Cartesian grid for axial piston pump

axial piston pump with spherical oil film built by the above manner is shown in Figure 2. The C program to extend PumpLinx is as follows:

$$
\begin{aligned}
r_{\text{sphere}} &= R \\
r_{\text{range}} &= L^2 \\
r_{xy} &= x^2 + y^2 \\
r_{\text{mod}} &= \left(r_{xy} > r_{\text{range}}\right) ? r_{\text{range}} : r_{xy} \\
\text{d}z &= r_{\text{sphere}} * \left(r_{\text{sphere}}^2 * r_{\text{mod}}\right)^{0.5} \\
z\text{new} &= z - \text{d}z
\end{aligned}
$$

The coordinates are related to the original center set by the user. The position of the coordinate origin is shown in Figure 2. The following coordinate system is established as according to the origin. $R$ is the spherical radius and $L$ is the diameter of the outer edge of the distribution plate. The oil film thickness was set to 10 μm, and the number of mesh layers was set to 5 to describe the gap leakage.

In addition, during the meshing process, mesh refinement was carried out on the valve plate surface and the two triangular relief grooves which contacted with the dynamic mesh of the piston.

### 2.3 Boundary Conditions and Model Parameter

The "Inlet" shown in Figure 2 is set as the pressure inlet boundary condition (0.1 MPa); the "Outlet" is set as the pressure outlet boundary condition (30 MPa). Mismatched grid interface (MGI) exists between the Inlet/Outlet port and the valve passages, the valve passages and the spherical oil film fluid domain, and the spherical oil film fluid domain and the piston assembly. The MGI surface is used to simulate the fluid transmission between different fluid domains. Considering the leakage between the inner and outer edges of the spherical oil film, the edges is set as the pressure outlet boundary condition (2 MPa). Except for the inlet/outlet boundary and MGI, other boundaries are uniformly set as solid wall surfaces. Although the liquid flow in the pump body is mostly considered as turbulent, the flow near the solid wall is mostly laminar. Therefore,RNG $k$-$\varepsilon$ model with low Reynolds number flow viscosity analytical equation is adopted in the simulation model.

The inclination angle of swash plate of piston pump is set to the maximum allowable angle (15°), and other relevant simulation parameters are shown in Table 1. In the simulation software, the time step for each piston rotation is set to 40 steps, and there are 9 piston chambers. The time step for on rotation cycle is 360 steps, in other words, the piston chamber rotates 1° for each step. In order to obtain the simulation results during stable period, the simulation was conducted for 5 steps in advance and the simulation results for the sixth steps were taken for research.

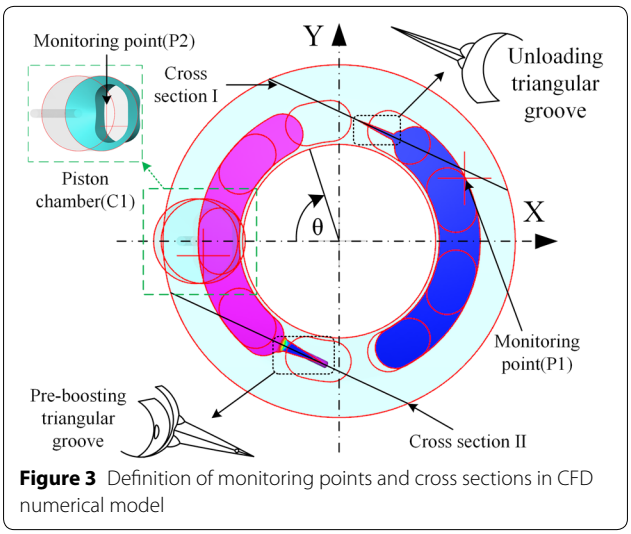


**Figure 3** Definition of monitoring points and cross sections in CFD numerical model

### 2.4 Mesh Sensitivity Analysis

The accuracy of the grid directly determines the accuracy level of the calculation. In order to determine the optimal grid size, 6 sets of calculation models are obtained by setting different grid parameters. The accurate calculation model will have a smaller flow rate error ($\Delta Q\%$). The flow error is calculated using the following equation:

$$\Delta Q\% = \frac{|Q_{\text{inlet}} - Q_{\text{outlet}}|}{Q_{\text{outlet}}} \times 100\%, \tag{14}$$

where $Q_{\text{inlet}}$ and $Q_{\text{outlet}}$ are the import and export flow rate, respectively.

The six sets of different mesh models are calculated on a computer with 16 cores and 32 Gb RAM. Each three

**Table 1 Model simulation parameter settings**

| Parameter | value |
|---|---|
| Liquid density (kg/m$^3$) | 865 |
| Rotational speed (r/min) | 1500 |
| Valve plate deflection angle $\psi_0$ (°) | 5.5 |
| Spherical radius of curvature (mm) | 396 ± 0.3 |
| Temperature (K) | 313.15 |
| Dynamic viscosity (Pa·s) | $4.464 \times 10^{-5}$ |
| Saturation pressure (MPa) | 0.004 |
| Liquid bulk modulus (MPa) | $1.5 \times 10^3$ |
| Gas mass fraction | $9 \times 10^{-5}$ |
| Gas molecular weight | 28.97 |
| Vapor molecular weight | 300 |

sets of calculations run at the same time, which takes 5 to 7 days. After about two weeks, the simulation results and corresponding flow errors of each group of grid model are obtained. The specific grid parameters and corresponding flow errors are shown in Table 2.

According to Table 2, improving the grid size and critical boundary angle can reduce the error between the suction and delivery flow. In the actual simulation process, the calculation time of the sixth sets of models is obviously longer, however, the flow error value does not decrease significantly. In order to achieve the best compromise between accuracy and calculation time, the fifth group of parameters is finally selected to generate the model.

## 3 Simulation Results and Analysis

In order to obtain the detailed flow field parameters and flow field cloud map distributions of the specified position or section in the piston pump, the observation points and cross sections are added in the CFD simulation model, and their positions are shown in Figure 3. The observation point 1 ($P1$) is set at a position where the unloading triangular groove faces the valve plate inner wall surface and is close to the spherical oil film in the $Z$ direction. The observation point 2 ($P2$) is set in the kidney-shaped port of the cylinder and is close to the rear wall surface. Due to the fluid field of the piston chamber rotates around the rotating shaft by using a moving grid, the motion equation of the point $P2$ is set according to the UDF motion function to make it move synchronously with the piston chamber. Therefore, the data at the point $P2$ can be collected in real-time, the trajectory of $P2$ is expressed as follows:

$$x_{P2} = R_0 \times \cos((2\pi \mathrm{n}/60) \times \mathrm{time} + \varphi_0),$$
$$y_{P2} = R_0 \times \sin((2\pi \mathrm{n}/60) \times \mathrm{time} + \varphi_0),$$
$$z_{P2} = 0.021,$$

where $R_0$ is the distance from the point $P2$ to the origin, n is the rotor speed, $\phi_0$ is the initial phase, and $z_{P2}$ is the vertical height from the original center.

In addition, cross sections I and II are respectively created along the opening direction of the two triangular grooves and perpendicular to the $Z$ axis, as shown in Figure 3. In order to elaborate evolution mechanism of cavitation erosion in detail, under the condition that the inlet/outlet mass flow error is less than 0.5%, the hydrodynamic parameters at each observation point and cross section are analyzed, such as fluid velocity and velocity vector diagram, gas volume fraction (GVF), gas volume fraction cloud image, and pressure field.

### 3.1 Submerged Jet at Unloading Triangle Groove

According to the simulation settings, the negative direction of the $X$-axis in Figure 3 is assumed as the initial position of the rotor ($\theta = 0°$). The piston chamber 1 (C1) is taken as the research object, and its position is shown in Figure 3. The point C1 starts from the initial position and contacts with the unloading triangular groove after it rotates 84° clockwise. The values of the following parameters are obtained by the relationship between the rotational speed and the angular velocity. The angular velocity (expressed by $\omega = 2\pi n/60$) is 50π revolutions per second and the period (expressed by $T = 2\pi/\omega$) is 0.04 s. The measured farthest distance (expressed by L) between the piston wall and the rotor center is 0.0585 m. Therefore, the outermost linear velocity of the piston chamber (expressed by $v = \omega L$) is about 9.189 m/s.

Figure 4 shows the variation of fluid velocity and gas volume fraction (GVF) at point $P1$. The principal longitudinal coordinate is the resultant velocity in the $X$ and $Y$ directions. Because the velocity in $Z$ direction has little effect on bubble collapse, it can be ignored. In Figure 4, the velocity of point $P1$ undergoes a sharp fluctuation for 9 cycles. The reason is that each piston passes through the triangular groove and causes a sharp change in the velocity at the observation point. Furthermore, the velocity peak value is much higher than the rotor rotation speed. The value of GVF at point $P1$ changes with the same frequency as the velocity, but slightly lags behind

**Table 2 Mesh sensitivity**

| Parameter | Group | | | | | |
|---|---|---|---|---|---|---|
| | 1 | 2 | 3 | 4 | 5 | 6 |
| Critical edge angle | 30 | 30 | 30 | 25 | 15 | 15 |
| Curvature resolution | 35 | 35 | 35 | 30 | 20 | 20 |
| Maximum cell size | 0.03 | 0.025 | 0.02 | 0.02 | 0.02 | 0.01 |
| Cell size on surfaces | 0.015 | 0.0125 | 0.01 | 0.01 | 0.01 | 0.005 |
| Number of cells | 150404 | 171800 | 180163 | 185882 | 294155 | 414843 |
| $\Delta Q$ (%) | 6.91 | 4.23 | 2.06 | 1.30 | 1.08 | 0.92 |

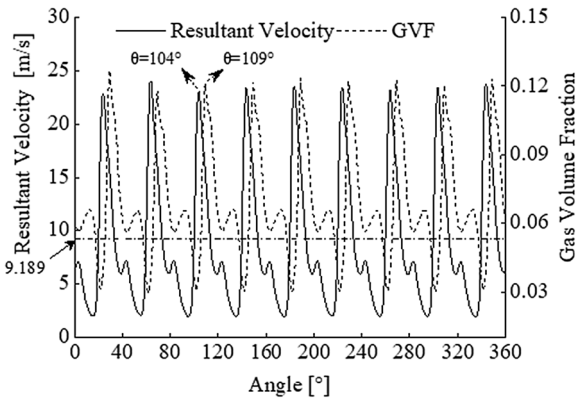


**Figure 4** Point *P*1 fluid velocity and gas volume fraction change

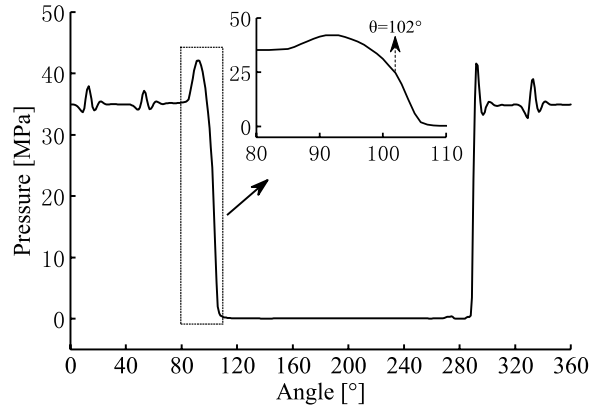


**Figure 6** Pressure change in the piston chamber C1

the velocity. The reason is that the fluid flow velocity is always faster than that of the gas flow under the high-speed jet carrying bubbles.

Figure 5 shows the pressure relief process of the residual high-pressure oil in C1 of the triangular groove. When the cylinder rotates for one cycle, the pressure variation in chamber C1 is shown in Figure 6. When $\theta = 84°$, the C1 is not connected to the unloading triangle groove. At this time, the fluid pressure in the chamber is about 30 MPa. As shown in Figure 6, reason for the pressure overshoot is that C1 is out of contact with the oil outlet and the volume of the piston chamber is reduced along with the piston moving downward. The cylinder is rotated from 85° to 101°, the cross-sectional area of the triangular groove increases from 0 $mm^2$ to 1.41 $mm^2$, which is the first stage unloading of residual high-pressure oil. During the first stage unloading process, C1 maintains a high pressure of 30 MPa; when $\theta = 102°$, C1 begins to contact with the ball slot, the cross-sectional flow area increases rapidly to 6.56 $mm^2$, and the second stage unloading begins until $\theta = 106°$ complete unloading.

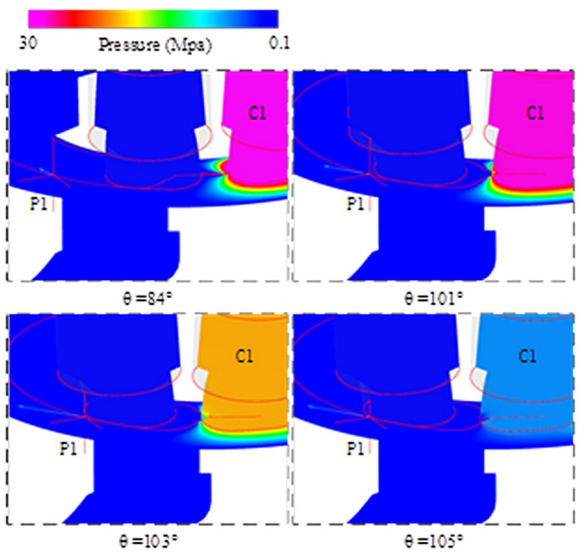


**Fig. 5** Evolution of pressure cloud diagram on cross section I and spherical oil film

During the first unloading stage, the triangular unloading groove acts as a jet "nozzle". The upstream is connected with high-pressure oil while the downstream is connected with the oil inlet of the valve plate. Due to the extremely high-pressure difference between the upstream and downstream, the oil in C1 will jet into the valve plate with extremely high speed. When the high-speed jet is injected into the static liquid domain, shear force (the shear force depends on the velocity gradient) will be generated between them, which will lead to the generation of the vortex. The vortex will generate an axial symmetry low pressure. The low pressure will lead to the formation of an annular cavitation cloud around the jet. The evolution process of submerged cavitation jet velocity caused by unloading triangular groove is shown in Figure 7.

The shape of the "nozzle" is shown as $\theta = 90°$, and the opening degree of the "nozzle" increases along with the rotor rotation movement. During the process of $\theta = 84°$–$93°$, the length of "nozzle" is the distance between the front and rear boundaries of two adjacent waist-shaped grooves of the cylinder body. According to Hitoshi Soyama [32], the distance meets the effective length (2.25 mm) of "nozzle" for forming a high-speed submerged jet. During the process of the rotor turning to $\theta = 102°$, the length of the "nozzle" gradually decreases to 0 mm. Therefore, in the range of $\theta = 84°$–$102°$, the jet formed in the unloading process of C1 can be considered as a continuous jet. For continuous jet flow, the cavitation bubbles generated in the initial vortex ring will be

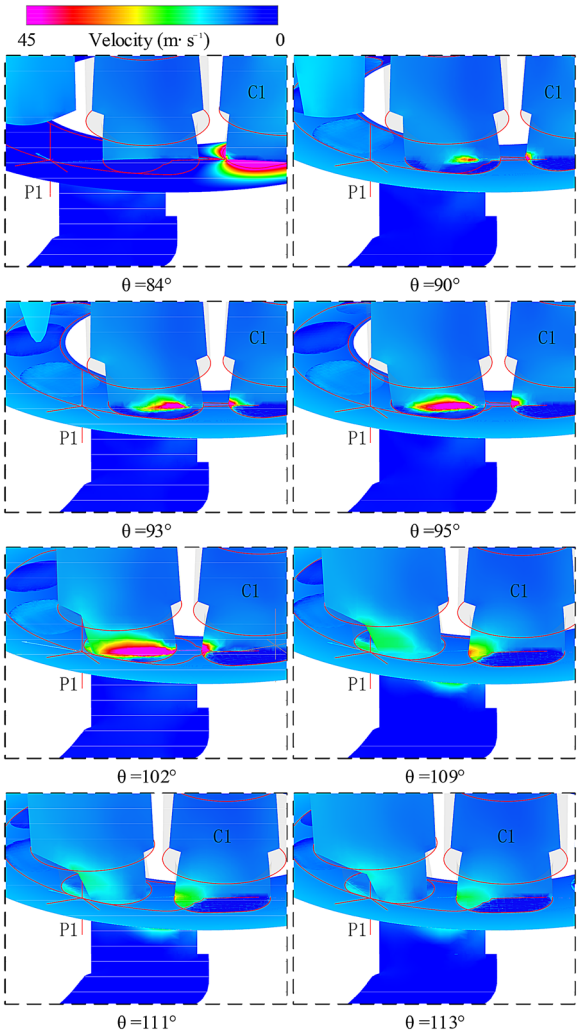


**Figure 7** Velocity nephogram on cross section I and spherical oil film and velocity vector change at point *P*1

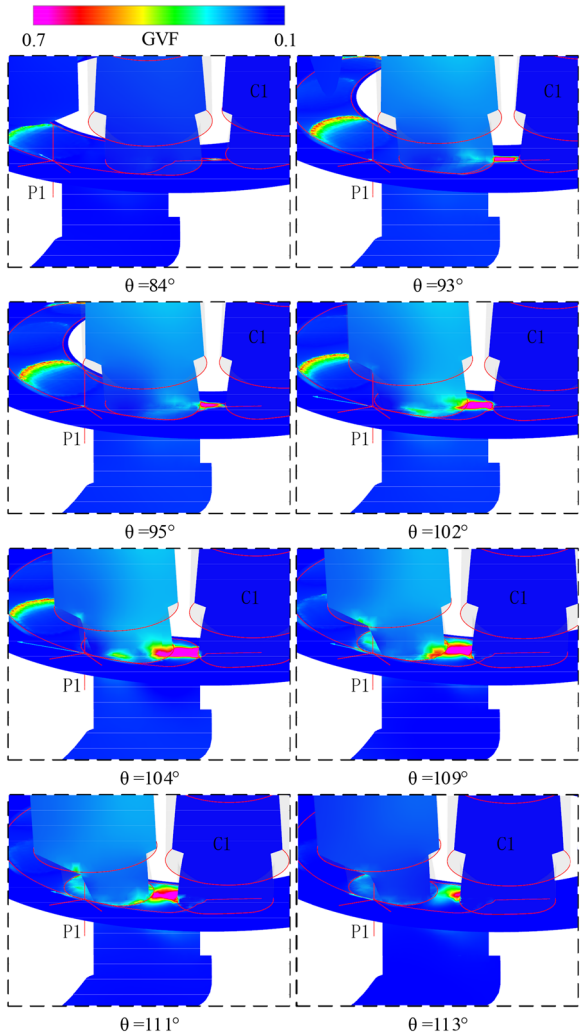


**Figure 8** Gas volume fractional cloud diagram on cross section I and spherical oil film

connected with the generating bubble ring subsequently. The bubbles will move downstream with the jet flow and survive within a certain distance. As shown in Figure 7, in this continuous process, after the velocity vector of point *P*1 increases gradually, the velocity basically remains unchanged in the process of $\theta = 104°–113°$.

The gas volume fraction cloud image at eight different times on section I and spherical oil film is shown in Figure 8. The velocity vector of point *P*1 is also shown in the Figure. The gradual evolution process of cavitation submerged jet along with the change of "nozzle" during the rotation of the rotor $\theta = 84°–102°$ is also illustrated in Figure8. When $\theta = 104°$, the submerged jet reaches the point *P*1, and reaches the wall of the distribution plate when $\theta = 109°$. The cavitation cloud follows the movement of the submerged jet.

As shown in Figure 9, the above phenomenon is closely related to the structure of spherical valve plate pair. Spherical valve plate pair makes the opening direction of the triangular groove change from obliquely downward

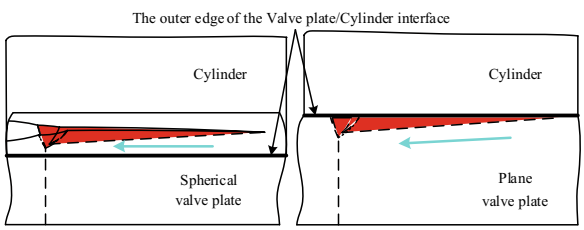


**Figure 9** Comparison of the triangular grooves in the interface between the spherical surface and the plane

to horizontally forward, causing the direction change of the fluid velocity vector flowing through the triangular groove. The spherical valve plate/cylinder block pair forms the height difference between the valve plate and the cylinder body between the outer edge and the inner edge, which makes the triangular groove opening only aligned with the valve plate inner wall surface become that the triangular groove opening faces the interface between the valve plate and the cylinder body.

It is also known from Figure 6 that, when the gas volume fraction at point *P*1 reaches the peak value (e.g., $\theta = 109°$), the speed of point *P*1 is higher than the linear speed of the outermost edge of the rotor. The cavitation cloud will directly jet to the inner wall surface of the valve plate along with the high-speed flow. The cavitation cloud will also hit the front end surface of the previous piston chamber. According to the data at point *P*1, it can be seen that the velocity at point *P*1 decreases sharply after the impact, and the gas volume fraction also decreases due to the impact between the cavitation cloud and wall surface. The phenomenon also can be found by the change trend of the velocity at the observation point and GVF curve in Figure 3.

### 3.2 Submerged Jet at Pre-boosting Triangular Groove

Figure 10 shows the variation of fluid velocity and GVF at point *P*2. Due to the point *P*2 written in the UDF function is rotated in synchronization with C1, the speed at the point *P*2 only fluctuates one time during one rotation cycle of the rotor. The GVF at point *P*2 has also increased when $\theta = 105°$, and maintains a certain gas content until C1 connects with the pre-boosting triangular groove. The main reason is that the C1 passes through the unloading triangle groove to complete the unloading during this process. The bubble that has not collapsed is sucked into C1, and the cavitation bubble generated by the next piston cavity unloading is also jeted into C1. Figure 8 confirms the process of bubble transfer and periodic circulation in the connected product.

The pressure cloud changes at four different moments in Section II are shown in Figure 11. The Figure 11 shows the whole boosting process of C1 from contacting the pre-boosting triangular groove to the small hole and then to the ball groove. The pressure change in the C1 cavity during one rotation cycle of the cylinder is shown in Figure 12. During the process of the rotor turning from 263° to 288°, the cross-sectional area of the triangular groove increases from 0 $mm^2$ to 10 $mm^2$. Although the piston chamber is pre-boosted, the volume of the cavity is gradually increased at this time, and the pressure in the chamber is not significantly improved. There is still an utmost

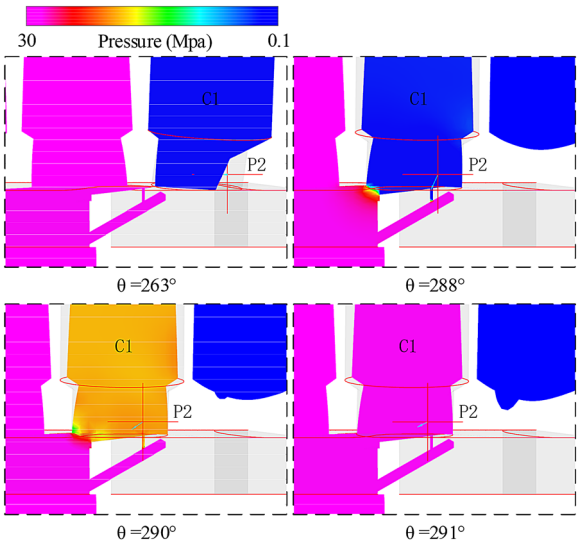


**Figure 11** Evolution of cross section II pressure cloud map

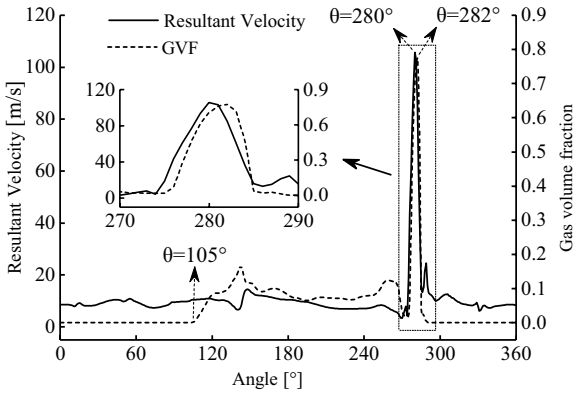


**Figure 10** Variation of point *P*2 fluid velocity and gas volume fraction

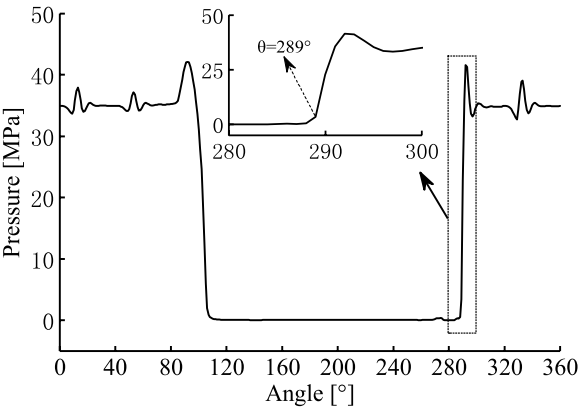


**Figure 12** Pressure change in the piston chamber CI

high pressure difference on the oil outlet. Until the piston chamber is completely connected with the ball groove, the flow area increases, and the pressure in the chamber rises sharply to the load pressure, as $\theta = 290°$ shown in Figure 11. The phenomenon indicates that the pre-boosting triangular groove is consistent with the unloading triangular groove in the process of $\theta = 263°$–$288°$. The pre-boosting process also has a jet effect, and the continuous jet will lead to the generation of cavitation cloud.

Figure 13 shows the changes of velocity cloud map and vector at eight different moments in cross-section II. During the process of $\theta = 263°$–$266°$, the effective length of the "nozzle" is from the small hole to the top of the triangular groove. At this moment, the "nozzle" opening is small and the jet phenomenon is not obvious. When the front end of the piston chamber passes over the small hole, during the process of $\theta = 267°$–$273°$, the length of the "nozzle" is still the distance between the front and rear boundaries of the adjacent two kidney grooves. During this process, the jet will be impacted by the fluid in the small hole. The velocity cloud diagram in Figure 13 shows that the small hole has little effect on the jet velocity. The jet still impinges on the inner wall of the cylinder near point *P*2. The jet velocity reaches its peak value when $\theta = 280°$. After the jet impacts the wall, the velocity vector direction changes, and the speed decreases.

Figure 14 shows the changes of the GVF cloud map and velocity vector at eight different moments in the cross-section II. The GVF cloud image of Section II shows that the bubbles spreads not only in the direction of the jet. This shows that although the jet velocity is less affected by the small orifice flow, the cavitation cloud is impacted by the small hole flow. The cavitation cloud is split into two parts into the piston cavity. One part is affected by

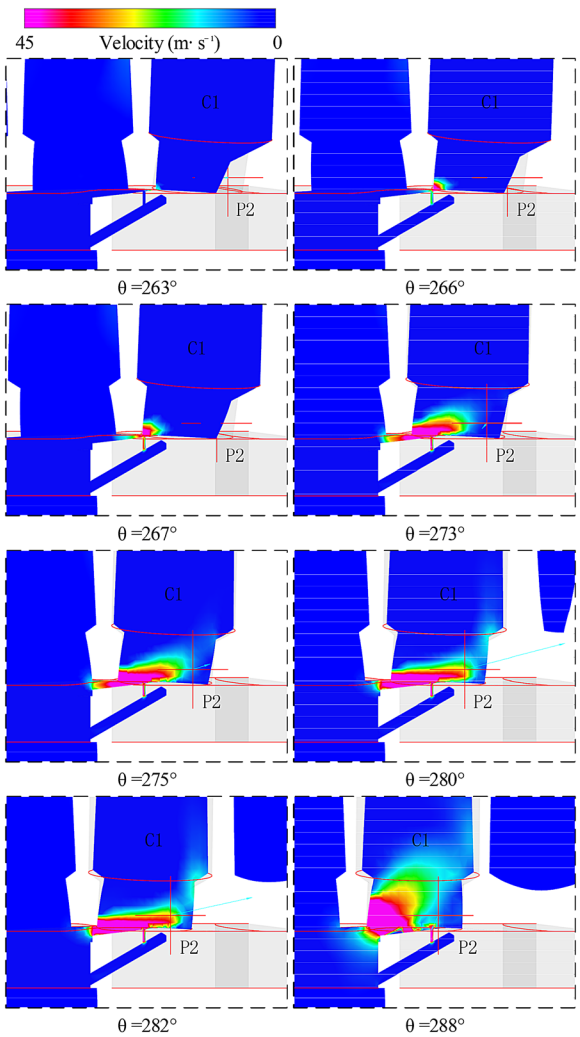


**Figure 13** Changes of cross section II velocity cloud map and velocity vector at point P2

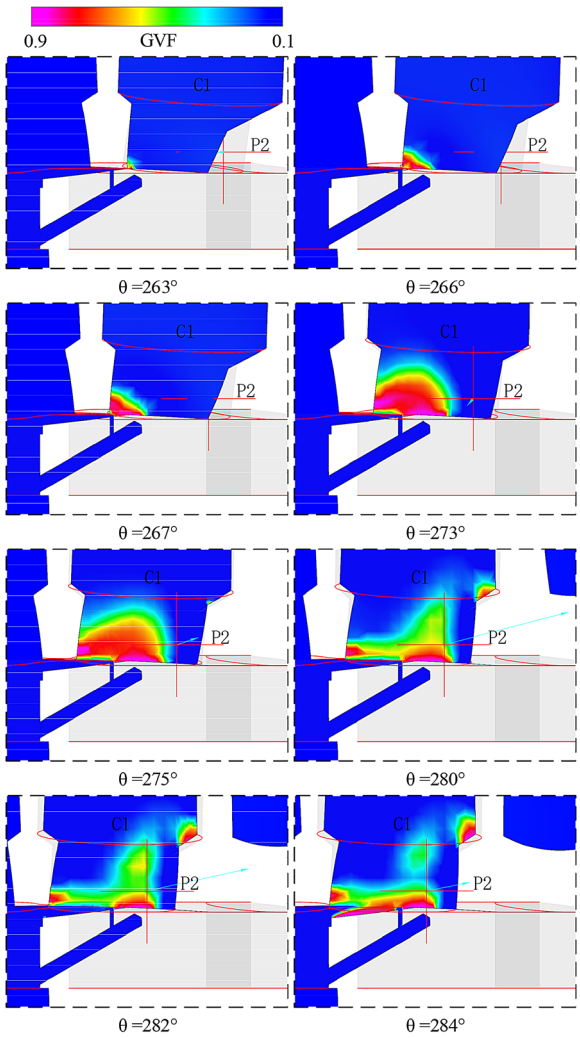


**Figure 14** Gas volume fractional cloud on cross section II

the pre-boosting triangle groove jet to impact on the inner wall surface of the kidney groove of the piston cavity. The other part is affected by the small hole and the triangular groove jet to impact on the inner wall surface of the piston chamber.

It can be seen from Figure10 that the GVF at the point P2 reaches peak value at $\theta = 282°$. The value decreases as the liquid flow backflow impinges on the wall surface of the kidney groove. As the continuous rotation movement of the cylinder rotor, the pressure in the piston chamber increases sharply, and the cavitation bubbles generated by the pre-boosting triangular grooves will collapse into the piston chamber, resulting in vibration and noise.

## 4 Discussion

Due to some characteristics of the structure of the spherical valve plate/cylinder block pair, the shape of the triangular groove is affected by the spherical surface. The two ends of the triangular groove tend to be the same horizontal height. There is a height difference between the left and right sides of the triangular groove, and the opening degree of the triangular groove is smaller than that of the triangular groove arranged in the plane. Cavitation phenomenon of variable shape triangular grooves is studied through durability life experiments. In order to reduce the experimental time, the piston pump operates continuously under the rated working conditions: the inlet pressure is set to 0.1 MPa, the oil suction port is fed with ISO VG 46 oil at 40 5 °C, and the pressure at the oil outlet is 30 MPa. The piston pump runs continuously for 1500 h with the rated speed of 1500 r/min.

Due to the continuous high load operation of the pump, in order to ensure the safety of the experiment and maintain the purity of the oil, the oil outlet is equipped with a filter. The oil passing through the filter is directly connected to the cooling tank, so that the oil can be recycled without increasing the oil temperature. Of course, the piston pump has also taken refrigeration measures, and cooling tap water is circulated to cool its shell. After the experiment was completed, the pump was disassembled, and the cavitation phenomenon shown was found in the valve plate and piston cylinder as shown in Figure 15.

According to the transient analysis of the rotation of the piston chamber C1 and combining with the changes of the gas volume fraction and velocity vector at points *P*1 and *P*2 (i.e., the erosion zone in Figure 15), it can be seen that cavitation cloud does impact the valve plate and the inner wall surface of the cylinder body. Figure 16 shows the cloud chart of gas volume fraction at the formation moment of cavitation.

By carefully observing the valve plate and the cylinder body, it can be found that there are erosion marks not only on the inner wall of the waist-shaped groove at the oil outlet of the valve plate facing the triangular groove, but also on the waist-shaped groove inner wall and the

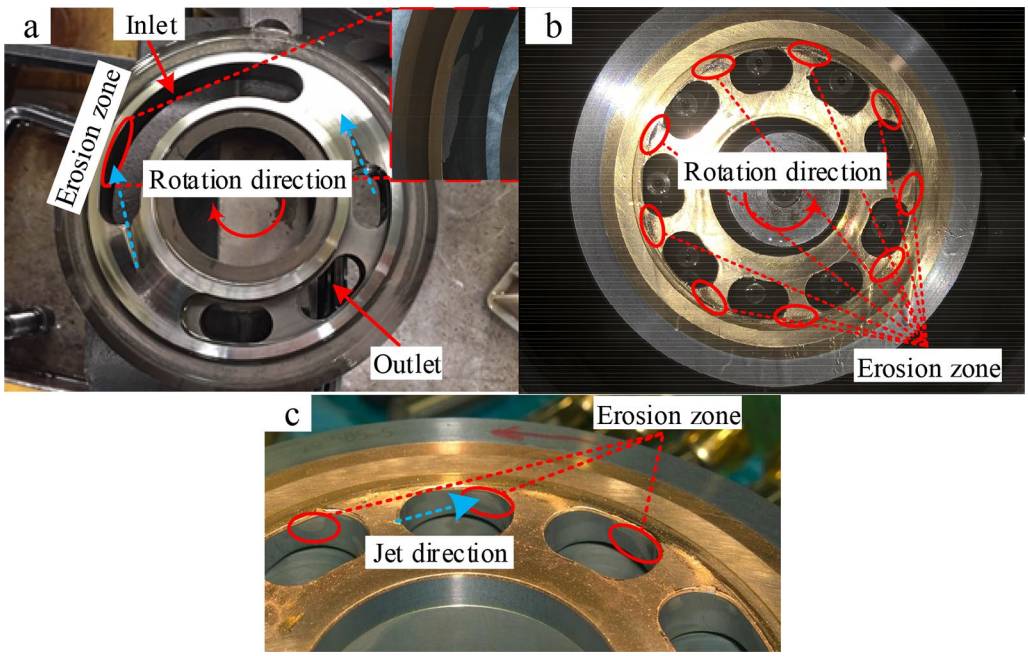


**Figure 15** Experimental cavitation photos of the spherical interface: **a** Cavitation damage map on the upper end of the valve plate, **b** Cavitation damage on the lower surface of the cylinder block, **c** Cavitation damage on the sidewall surface of the kidney trough of cylinder block

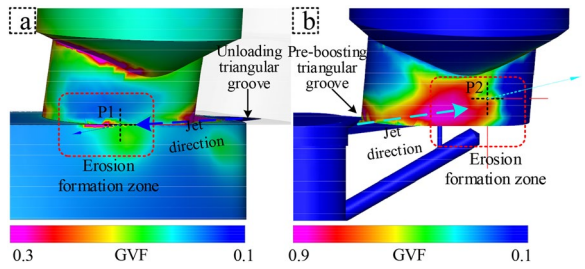


**Figure 16** Formation moment of cavitation erosion

lower end surface of the cylinder body. In addition, the erosion trace direction at the spherical valve plate/cylinder block pair is along the rotation direction of the rotor. The erosion position is on the outer wall surface far away from the center of the rotor, and the erosion occurs on the upper and lower sides of the spherical pair. By comparing Figure 15 with Figure 16a, it is shown that the positions of cavitation area obtained by experiment and simulation are consistent. The velocity direction at observation point *P*1 is consistent with the jet direction of unloading triangular groove. Therefore it is concluded that the erosion of inner wall of the kidney groove of the valve plate oil suction side and the lower bottom surface of cylinder body is caused by the impact of cavitation cloud cluster ejected from unloading triangular groove at time of the Figure 16a.

The direction of the erosion marks on the inner side wall of the kidney groove of the cylinder body is opposite to the rotation direction of the rotor. By comparing Figure 15c with Figure 16b, it is shown that the position of cavitation erosion area obtained by experiment and simulation is consistent, and the velocity direction at observation point *P*2 is consistent with the jet direction of pre-boosting triangular groove. It's proved that the erosion of the inner wall surface of the cylinder waist groove is caused by the backward submerged cavitation jet generated by pre-boosting triangular groove at time of Figure 16b. The submerged cavitation jet generated by the pre-boosting triangular groove is affected by the liquid flow of the small hole. The damage degree of cavitation cloud on the inner wall of the waist groove will be slightly smaller than that on the inner wall surface of the valve plate and the lower surface of the cylinder body, as shown in Figure 15c.

By comparing the simulation results with the experimental data, the cavitation prediction accuracy of the numerical model is verified. The results show that submerged jet at unloading triangular groove and pre-pressure boosting triangular groove are important inducers for cavitation of the piston pump. The cavitation cloud will survive in a certain distance under the influence of fluid velocity, resulting in impacting on the solid surface. Refs. [28, 29] show that when the cavitation cloud jet reaches the wall, the cavitation flow will undergo a rapid phase change near the target wall, and some bubbles burst directly or become smaller bubbles when they hit the solid surface at high speeds. Under the influence of bubble rupture, the local pressure rises sharply, which makes the nearby bubbles to deform and combine with other bubbles or suffer oscillation rupture. Then the phenomenon will continue, resulting in superposition of energy near the wall. The energy can be divided into normal and tangential directions. The normal stress causes plastic deformation of the piston chamber wall. The tangential force causes bubbles to diffuse or to be transported downstream. Bubbles rupture at a certain downstream point causes a larger area of plastic deformation, which is the incubation period of erosion. As time passes, the damage caused by cavitation goes beyond the plastic deformation, and the material in the erosion zone is removed. The longer the time takes, the more behavior will be sustained the behavior.

## 5 Structure Optimization of Valve Plate

For the special cavitation phenomenon in the cylinder and the valve plate of the piston pump with spherical interface, the orientation of unloading triangular groove is modified to relieve the jet erosion on the lower surface of cylinder body and the inner wall surface of valve plate. In this way, the wear of spherical valve plate pair can be reduced.

Professor Ezddin Hutli at Institute of Nuclear Techniques, Budapest University of Technology and Economics, has studied submerged cavitation jets. He concludes that when the length of submerged cavitation jets is equal to the standoff distance (the distance of jet nozzles according to the target surface to be impacted), there is an optimal standoff distance. The nozzle under this condition has the highest erosion efficiency [29]. On the contrary, if the confrontation distance is greater than the cavitation cloud length, the longer the confrontation distance is, the lower the erosion efficiency of the nozzle becomes. Based on this theory, we improved the unloading triangular groove structure of the valve plate. The improved distribution plate structure is shown in Figure 17.

In order to extend the confronting distance between the unloading triangular groove and the inner wall surface of the valve plate, the triangular groove angle is rotated clockwise around the original triangular groove vertex without changing the vertex position and opening degree of the triangular groove. If the confrontation

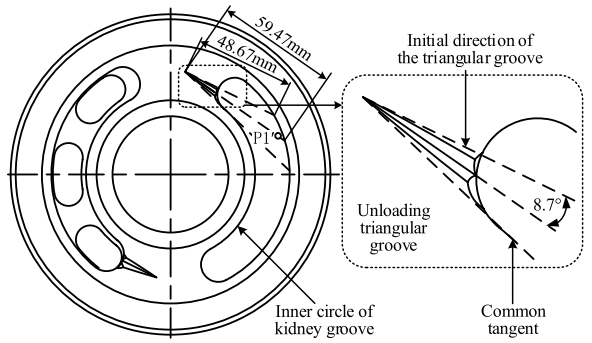


**Figure 17** Improved valve plate structure

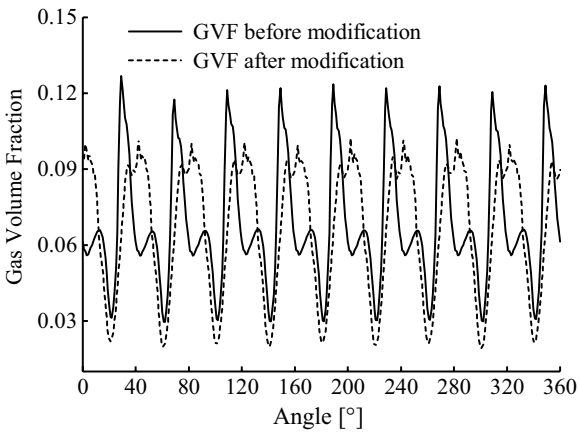


**Figure 18** Comparison of GVF at observation points with and without structure modification

distance reaches the achievable limit length, a common tangent line exists between the ball groove at the opening of the triangular groove and the inner circle of the kidney groove of the valve plate. The center line of the improved valve plate triangular groove is deflected by 8.7° from the original center line of the triangular groove, and the confrontation distance is prolonged by 10.8 mm.

Because the establishment of the fluid domain model is carried out by importing STL files of each fluid domain into PumpLinx separately, only the modified valve plate fluid domain needs to be used to replace the original valve plate fluid domain. The grid encryption area corresponding to the original valve plate performs grid encryption on the improved distribution plate. The other relevant model parameters and boundary condition settings remain unchanged. It can not only control variables effectively, but also save a lot of modeling time.

For the post-processing of the model, the observation point $P1$ is shifted with the $Z$ coordinate, so that it is still near the inner wall surface of the valve plate and aligned with the unloading direction of the unloading triangular groove. The position of the obtained point $P1'$ is shown in Figure 17. In order to obtain the data from the stable period of simulation results, the model is also simulated for 5 rounds in advance, and the simulation data of the sixth cycle are taken as the simulation results to compared with those of the un-modified structure. The comparison results of the gas volume fraction extraction are shown in Figure 18. The simulation results show that the gas volume fraction of the valve plate facing the triangular groove opening is reduced by about 20% for the modified valve plate.

The biggest difference between submerged cavitation jet and free jet is the shear stress which occurs between the jet and the surrounding stop liquid [29]. Therefore, the longer the confrontation distance is, the greater the influence of shear stress on the jet becomes. The shear stress will significantly affect the jet velocity and the motion direction of cavitation cloud. By intercepting the gas volume fraction nephogram as shown in Figure 19 when submerged cavitation jet reaches the inner wall surface of the valve plate, and comparing with the gas volume fraction nephogram as shown in Figure 16a, it is concluded that cavitation cloud clusters appear obvious dispersion. Under the influence of shear force, the velocity vector length at point $P1'$ is significantly shorter than that in Figure 16a. The phenomenon indicates that the jet velocity reaching the wall surface is significantly reduced, greatly alleviating the strong erosion of submerged jet on the wall surface of parts.

## 6 Conclusions

(1) A three-dimensional simulation model that can predict cavitation characteristics of a piston pump with spherical valve plate is established. The three-dimensional hydrodynamic model for CFD simulation is improved by refining the key structure grid, compiling the oil membrane structure with UDF

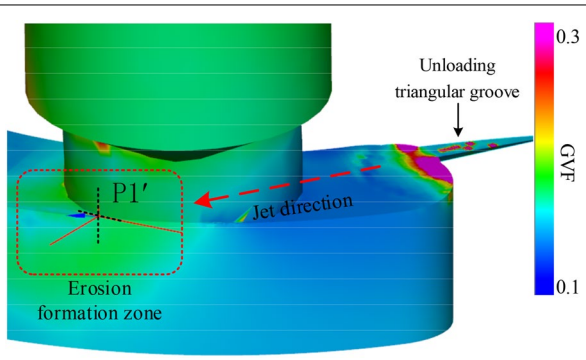


**Figure 19** Moment of cavitation erosion

function, and adding a motion model to simulate the high-speed operation of the piston pump. Finally, the reliability and accuracy of the numerical model is evaluated and verified by the best consistency between numerical prediction and durability test data.

(2) The research results show that the erosion of the valve plate and cylinder block in the axial piston pump with spherical valve plate is caused by submerged cavitation jet. The formation of submerged cavitation jet depends on the formation of "nozzle", the opening of "nozzle", and the pressure difference between upstream and downstream of "nozzle". The erosion damage caused by cavitation submerged jet is closely related to jet angle and confrontation distance (distance from nozzle to target wall). By improving the structure of the distribution plate, i.e., prolonging the confrontation distance, the erosion effect of submerged cavitation jet on the wall surface of parts is obviously improved The research provides a valuable analysis method for the engineering design of the valve plate of the piston pump and the performance improvement of the pump in the future.

**Acknowledgements**
Not applicable.

**Authors' contributions**
BZ and LQ was in charge of the whole trial; WG wrote the manuscript. All authors read and approved the final manuscript.

**Authors' Information**
Bin Zhao, born in 1981, is currently a master's tutor and an associate professor at *Taiyuan University of Technology, China*, mainly engaged in electromechanical equipment modeling theory and intelligent control, electro-hydraulic energy-saving systems, hydraulic components.

Weiwei Guo, born in 1993, is currently a master candidate at *College of Mechanical and Vehicle Engineering, Taiyuan University of Technology, China*.

Long Quan, born in 1959, is currently a professor and a PhD candidate supervisor at *College of Mechanical and Vehicle Engineering, Taiyuan University of Technology, China*. His main research interests include vibration noise analysis and control, impact protection theory and application, and modern vibration isolation and vibration reduction methods.

**Funding**
Supported by National Natural Science Foundation of China (Grant No. 51605322), Shanxi Provincial Natural Science Foundation of China (Grant No. 201901D111054), International Cooperation Project of Shanxi Province (Grant No. 2016-002), and Key Laboratory of Fluid and Power Machinery, Ministry of Education (Grant No. GZKF-201815).

**Competing interests**
The authors declare no competing financial interests.

**Author Details**
[1] College of Mechanical and Vehicle Engineering, Taiyuan University of Technology, Taiyuan 030024, China. [2] Transducers and Intelligent Control System of Ministry of Education and Shanxi Province, Taiyuan University of Technology, Taiyuan 030024, China. [3] The State Key Laboratory of Fluid Power & Mechatronic Systems, Zhejiang University, Hangzhou 310027, China.

**Received: 13 November 2019 Revised: 29 August 2020 Accepted: 14 September 2020**
Published online: 01 October 2020

**References**

[1] A Lannetti, M T Stickland, Dempster W M. A CFD and experimental study on cavitation in positive displacement pumps Benefits and drawbacks of the full cavitation model. *Engineering Applications of Computational Fluid Mechanics*, 2016, 10(1): 57–71.
[2] R Amirante, E Distaso, P Tamburrano. Experimental and numerical analysis of cavitation in hydraulic proportional directional valves. *Energy Conversion and Management*, 2014, 87: 208–219.
[3] Z Rui, X C Hong. Numerical analysis of cavitation within slanted axial-flow pump. *Journal of Hydrodynamics*, 2013, 25(5): 663–672.
[4] J Zhou, A Vacca, P Casoli. A novel approach for predicting the operation of external gear pumps under cavitating conditions. *Simulation Modelling Practice and Theory*, 2014, 45: 35–49.
[5] E Frosina, A S Orcid, O A M Rigosi. Study of a high-pressure external gear pump with a computational fluid dynamic modeling approach. *Energies*, 2017, 10(8): 1113.
[6] G E Totten, Y H Sun, Jr R J Bishop. Hydraulic system cavitation: A review. *SAE Transactions*, 1998: 368–380.
[7] Q Chao. *Research on some key technologies of high-speed rotation for axial piston used in EHAs*. Hangzhou: Zhejiang University, 2019.
[8] E O T Kunimoto. Cavitation detection in the oil hydraulic equipments: Proceedings of the JFPS International Symposium on Fluid Power. *The Japan Fluid Power System Society*, 1996(3): 461–466.
[9] J J Zhou. *Study on cavitaion in multi-connected volumes and its effects on the operation of gear pumps*. Beijing: Beijing Institute of Technology, 2015.
[10] W K, Z K, M S, et al. Possibilities of diagnosing cavitation in hydraulic systems. *Archives of Civil and Mechanical Engineering*, 2007,7(1): 61–73.
[11] W Wustmann. *Experimentelle und numerische Untersuchung der Strömungsvorgänge in hydrostatischen Verdrängereinheiten am Beispiel von Außenzahnrad-und Axialkolbenpumpe.* Technische Universität Dresden, Institut für Fluidtechnik, 2010. (in Gemany)
[12] G Sravani, P Michael, Jennifer Kensler M C, et al. An investigation of hydraulic fluid composition and aeration in an axial piston pump. *Fluid Power Systems Technology, American Society of Mechanical Engineers*, 2017, 58332: V001T01A028.
[13] S Wang. The analysis of cavitation problems in the axial piston pump. *Journal of Fluids Engineering-Transactions of the ASME*, 2010, 132: 1-6.
[14] R J Bishop, G E Totten. Effect of pump inlet conditions on hydraulic pump cavitation: A review. *Hydraulic Failure Analysis: Fluids, Components, and System Effects. ASTM International*, 2001.
[15] F L Yin, S Nie, S L Xiao, et al. Numerical and experimental study of cavitation performance in sea water hydraulic axial piston pump. *Proceedings of the Institution of Mechanical Engineers, Part I: Journal of Systems and Control Engineering*, 2016, 230(8): 716–735.
[16] N Bügener, J Klecker, J Weber. Analysis and improvement of the suction performance of axial piston pumps in swash plate design. *International Journal of Fluid Power*, 2014, 15(3): 153–167.
[17] Z G Sun, S D Xiao, M H Xu, et al. Optimization of plunger cavity cavitation based on cylinder block kidney shape hole. *Journal of South China University of Technology (Natural Science Edition)*, 2016, 44(10): 35–41.
[18] H Kosodo. Development of micro pump and micro-hst for hydraulics. *JFPS International Journal of Fluid Power System*, 2012, 5(1): 6–10.
[19] M Zecchi, M Ivantysynova. Spherical valve plate design in axial piston machines—a novel thermoelasto-hydrodynamic model to predict the lubricating interface performance. *8th International Conference on Fluid Power Transmission and Control*, Hangzhou, China, 2013: 325–329.
[20] H Kosodo, M Nara, S Kakehida, et al. Experimental research about pressure-flow characteristics of V-notch. *Proceedings of the JFPS International Symposium on Fluid Power. The Japan Fluid Power System Society*, 1996(3): 73–78.
[21] S G Ye, J J Zhang, B Xu, et al. Experimental and numerical studies on erosion damage in damping holes on the valve plate of an axial piston

pump. *Journal of Mechanical Science and Technology*, 2017, 31(9): 4285–4295.
[22] X H Liu. *Study on the characteristic of cavitation erosion in hydraulic pump and valve*. Chengdu: Southwest Jiaotong University, 2008.
[23] X H Liu. Cavitaiton erosion mechanism of port plate of hydraulic axial plunger pump. *Journal of Mechanical Engineering*, 2008, 44(11): 203–208. (in Chinese)
[24] T Tetsuhiro. Visualized analysis of cavitation inside axial piston pump. *Chinese Gydraulice & Pneumatics*, 2015(2): 1–7.
[25] Y Shi, T Lin, G Meng, et al. A Study on the suppression of cavitation flow inside an axial piston pump. *2016 Prognostics and System Health Management Conference (PHM-Chengdu)*, IEEE, 2016: 1–5.
[26] K Toshiharu, K Kumagai, Y Osafune, et al. Erosion of grooved surfaces by cavitating jet with hydraulic oil. *Journal of Flow Control, Measurement & Visualization (JFCMV)*, 2015, 3(2): 41–50.
[27] E Hutli, S Aboyali, M B Hucine, et al. Influence of hydrodynamic conditions and nozzle geometry on appearance of high submerged cavitation jets. *Thermal Science*, 2013, 17(4): 1139–1149.
[28] E Hutli, M S Nedeljkovic, A Bonyárd, et al. Experimental study on the influence of geometrical parameters on the cavitation erosion characteristics of high speed submerged jets. *Experimental Thermal and Fluid Science*, 2017, 80: 281–292.
[29] E Hutli, M Nedeljkovic, A Bonyár. Cavitating flow characteristics, cavity potential and kinetic energy, void fraction and geometrical parameters – Analytical and theoretical study validated by experimental investigations. *International Journal of Heat and Mass Transfer*, 2018, 117: 873–886.
[30] V Yakhot, S A Orszag, S Thangam, et al. Development of turbulence models for shear flows by a double expansion technique. *Phys. Fluids A*, 1992, 4(7): 1510–1520.
[31] A K Singhal, M M Athavale, H Li, et al. Mathematical basis and validation of the full cavitation model. *Journal of Fluids Engineering*, 2002, 124(3): 617–624.
[32] S Hitoshi. Effect of nozzle geometry on a standard cavitation erosion test using a cavitating jet. *Wear*, 2013, 297: 89.